



Mud Density Optimization for Horizontal Well System in Clayey Silt Hydrate Reservoir with Considering Borehole Collapse

Qingchao Li¹

Received: 18 January 2021 / Accepted: 9 November 2021 / Published online: 6 January 2022
© King Fahd University of Petroleum & Minerals 2021

Abstract

Although horizontal well system has great advantages in methane production from clayey silt hydrate reservoir, borehole collapse is easy to occur during the drilling operation, which can seriously affect the drilling safety and efficiency. However, previous investigations have failed to thoroughly explore the mechanism of borehole collapse in horizontal well system. In this study, numerical investigation on collapse behavior of different boreholes within the horizontal well system in hydrate reservoir was conducted. It is found that borehole enlargement rate of both injection wells and production wells in horizontal well system decreases with the increase of drilling fluid density. However, due to the faster dissociation rate of natural gas hydrates, borehole enlargement rate is often higher in injection wells as compared to production wells. Based on the investigation results of borehole stability, lower limit of the safe mud weight window for horizontal well system was determined by considering different acceptable borehole enlargement rates. After analysis, it was found that the lower limit of the safe mud weight window depends on the mud density of the injection well for a specific acceptable borehole expansion rate. Moreover, the lower limit of safe mud weight window needs to be designed larger with improvement of the requirement for wellbore stability (i.e., decrease of acceptable borehole enlargement rate). For example, when acceptable borehole enlargement rate changes from 20 to 5%, the lower limit of the safe mud weight window needs to be increased from 1.007 to 1.047. Investigations in this paper will play a significant role in preventing serious borehole instability during drilling operation in hydrate reservoirs.

Keywords Hydrate deposits · Hydrate dissociation · Borehole collapse · Bottom-hole pressure · Drilling mud density · Reservoir deformation

Abbreviations

Az, Inc	Azimuth angle and inclination angle, degree	P_{eq}	Phase equilibrium pressure of methane hydrate, MPa
C_0	Initial cohesion of hydrate-bearing sediments, MPa	P_m	Bottom-hole pressure, MPa
C_1	Cohesion of sample without hydrate, MPa	P_p	Pore pressure, MPa
D	Depth below seafloor, mbsf	R_S, R_B	Stress transformation tensor
DT	Temperature disturbance front, m	S_h	Hydrate saturation, %
E_0	Elastic modulus of reservoir without hydrate, MPa	T	Temperature, K
g	Gravitational acceleration, 9.8 m/s ²	t	Drilling time, s
H	Water depth, m	V_t	Advancement rate of temperature disturbance front, cm/min
P_{atm}	Atmospheric pressure at sea level, MPa	ν	Poisson's ratio
		ν_0	Poisson's ratio before hydrate dissociation, 0.275
		α_1, α_2	Two Biot's coefficients, 1.25, 1.15
		α, β, γ	Three rotation angles, degree
		σ_B	Stress tensor in borehole coordinate system, MPa
		σ_P	In situ stress tensor, MPa
		$\sigma_H, \sigma_H, \sigma_H$	In situ stress components, MPa

✉ Qingchao Li
liqingchao2020@hpu.edu.cn; B16020053@s.upc.edu.cn

¹ School of Energy Science and Engineering, Henan Polytechnic University, Jiaozuo 454000, Henan, China



φ	Internal friction angle for samples with hydrate saturation of S_h
ϕ_0	Initial porosity of reservoir without hydrate, %
ρ	Average buoyant density of the sediment particles, Kg/m^3
ρ_{sea}	Density of sea water, 1030 kg/m^3

1 Introduction

In recent years, China has made remarkable achievements in economy, etc., but it depends on huge energy consumption (mainly fossil fuels such as oil and gas) [1]. Unfortunately, most of the oil fields in China are in high water-cut stage now, and the goal of stable production is difficult to be achieved [2, 3]. Currently, more than half of the crude oil required for society development in China need to be imported overseas [4, 5]; the external dependence on crude oil and natural gas reached 73% and 43%, respectively, in 2020. To ensure energy security, the exploration and development of unconventional oil and gas resources have been put on the agenda of the Chinese government. Among them, natural gas hydrate is a promising alternative to oil and gas resources [6].

Natural gas hydrates are solid crystalline formed by water and some gas molecules (methane accounts for more than 95%) at low temperature and/or high pressure in nature [7–13]. In fact, the global reserves of natural gas hydrates are $2.1 \times 10^{16} \text{ m}^3$, and the organic carbon stored in natural gas hydrates worldwide is about twice as much as that in traditional fossil fuels [8, 14–17]. At present, a variety of development methods have been put forward, including depressurization, thermal stimulation, CO_2 replacement and inhibitor injection [18]. However, cementation of marine hydrates is usually poor, and its strength can be severely affected by environmental changes [19, 20]. As shown in Fig. 1, affected by disturbance of drilling operation, borehole instability is one serious issue affecting drilling safety and subsequent gas production [21, 22]. Therefore, it is of great significance to carry out relevant investigations on borehole stability in hydrate reservoir for the efficient development of gas hydrates in the future [23–25].

Objectively speaking, theoretical investigations on wellbore stability during drilling operation in hydrate reservoir have been widely conducted in the past two decades, and some progresses have been made. However, related experimental studies are rare. In any case, all these investigations have made a significant contribution to exploring the mechanism of wellbore instability in hydrate reservoir. To name a few, Birchwood et al. [26] performed a numerical study on stress distribution and plastic strain area around the vertical borehole in hydrate reservoir with the semi-empirical formula, and it was found that accuracy of the investiga-

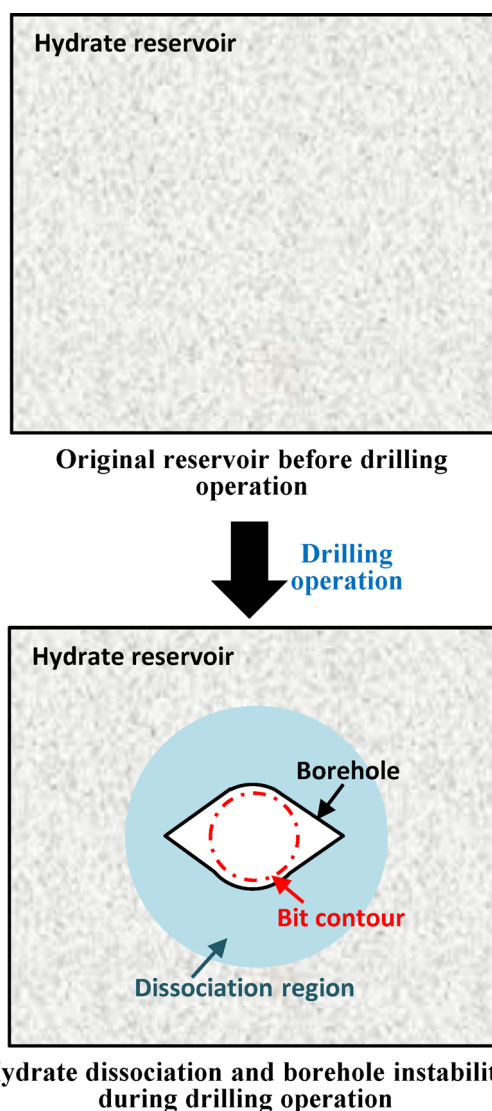


Fig. 1 Schematic of borehole instability caused by disturbance of drilling operation in hydrate reservoir

tion is high. In order to analyze borehole stability in hydrate reservoir, Freij-Ayoub et al. [27] inspected wellbore stability in hydrate reservoir by developing a coupling model, and borehole stability was comparatively investigated in hydrate deposits when different physical fields are taken into account. Salehabadi [28] numerically analyzed the integrity of casing in hydrate reservoir and found that the integrity of a centered casing deteriorated with the enhancement of thermal conductivity of cement, but it was just the opposite when the casing was eccentric. Li et al. [25] proposed an investigation method for simulating the vertical borehole collapse in clayey silt hydrate reservoir, and it was found that the established investigation model displayed obvious superiority.

As far as the authors know, current studies on wellbore stability in hydrate reservoirs mainly present the following

two shortcomings. Primarily, most of the investigations are conducted on vertical wells, and there are few analyses on stability of boreholes in horizontal well system. It should be noted that each well in horizontal well system interferes with each other during the drilling operation, and the borehole stability is significantly different from that of a single horizontal wellbore. Secondly, current investigations mostly focus on the regularity analysis of wellbore stability, and the corresponding engineering suggestions are rarely discussed.

The aim of this paper is to evaluate the stability of boreholes within horizontal well system due to hydrate dissociation and to present engineering measures for weakening the borehole instability. In order to achieve these two goals, a series of research work have been carried out. Firstly, collapse pressure for clayey silt hydrate reservoir in the northern South China Sea was determined based on the modified Mohr–Coulomb strength criterion when hydrate dissociation is neglected. However, natural gas hydrates around wellbore are likely to dissociate during drilling operation due to the disturbance of drilling fluid, thus affecting borehole stability. Therefore, the finite element model of a horizontal well system that contained three horizontal boreholes was established, and effect of drilling mud density on borehole collapse was then analyzed. Based on this, by considering different acceptable borehole enlargement rate, the lower limit of the safe mud weight window was optimized. Finally, the deformation response of hydrate-bearing sediments to drilling operation in hydrate reservoir was also evaluated.

2 Study Area and Exploration History

Shenhu area is the main playing arena for the Chinese government to carry out hydrate exploration activities in the South China Sea [11, 17, 29]. Figure 2 shows the geographical location of the study area. Shenhu area is affiliated to the Zhu II depression of the Pearl River Mouth Basin and geographically located between the Xisha Trough and the Dongsha Islands [30–33]. Although China has been exploring and developing oil and gas resources in this area for a long time, exploration activities targeting natural gas hydrate have only lasted for about 20 years. In 1999, China officially launched exploration activities on natural gas hydrates in the South China Sea [34, 35]. After that, four exploration activities were conducted by Guangzhou Marine Geological Survey in Shenhu area in 2007, 2013, 2015 and 2016, respectively [29, 36]. The exploration results show that prospective reserves of natural gas hydrates that equivalent to 68 billion tons of crude oil are expected to be contained in the South China Sea [37]. Moreover, natural gas hydrates in the northern South China Sea accounted for about 27.5% of the total reserves in the South China Sea [38]. In a nutshell, the total reserves of nat-

ural gas hydrates in study area are considerable, and it is of great significance to conduct relevant research.

3 Fundamental Theory

3.1 Effective Stresses Around Borehole

Considering the fact that both the inclination and azimuth of borehole are uncertain, in situ stresses in in situ stress coordinate system need to be transformed to borehole coordinate system before stress analysis of the rock around wellbore. Figure 3 shows the method of stress transformation between different coordinate systems. Effective stresses in borehole coordinate system can be obtained by Eq. (1) [39].

$$\sigma_B = \begin{Bmatrix} \sigma_B^{xx} & \sigma_B^{xy} & \sigma_B^{xz} \\ \sigma_B^{yx} & \sigma_B^{yy} & \sigma_B^{yz} \\ \sigma_B^{zx} & \sigma_B^{zy} & \sigma_B^{zz} \end{Bmatrix} = R_B R_S^T \sigma_P R_S R_B^T \tag{1}$$

R_S and R_B in Eq. (1) can be expressed by Eqs. (2) and (3).

$$R_S = \begin{Bmatrix} \cos\alpha \cdot \cos\beta & \sin\alpha \cdot \cos\beta & -\sin\beta \\ \cos\alpha \cdot \sin\beta \cdot \sin\gamma & \sin\alpha \cdot \sin\beta \cdot \sin\gamma & \cos\beta \cdot \sin\gamma \\ -\sin\alpha \cdot \cos\gamma & +\cos\alpha \cdot \cos\gamma & \\ \cos\alpha \cdot \sin\beta \cdot \cos\gamma & \sin\alpha \cdot \sin\beta \cdot \cos\gamma & \cos\beta \cdot \cos\gamma \\ -\sin\alpha \cdot \sin\gamma & -\cos\alpha \cdot \sin\gamma & \end{Bmatrix} \tag{2}$$

$$R_B = \begin{Bmatrix} \cos(Az)\cos(Inc) & \sin(Az)\cos(Inc) & -\sin(Inc) \\ -\sin(Az) & \cos(Az) & 0 \\ \cos(Az)\sin(Inc) & \sin(Az)\sin(Inc) & \cos(Inc) \end{Bmatrix} \tag{3}$$

Then, the effective stresses on borehole in cylindrical borehole coordinate system can be expressed as Eq. (4).

$$\begin{aligned} \sigma_r &= P_m - P_p \\ \sigma_\theta &= \sigma_B^{xx} + \sigma_B^{yy} - 2(\sigma_B^{xx} - \sigma_B^{yy})\cos 2\theta - 4\sigma_B^{xy}\sin 2\theta - P_m - P_p \\ \sigma_z &= \sigma_B^{zz} - 2\nu[(\sigma_B^{xx} - \sigma_B^{yy})\cos 2\theta + 2\sigma_B^{xy}\sin 2\theta] - P_p \\ \sigma_{\theta z} &= 2(\sigma_B^{yz}\cos\theta - \sigma_B^{xz}\sin\theta) \end{aligned} \tag{4}$$

Using Eqs. (1) to (4), the in situ stresses can be transformed from the in situ stress coordinate system to the borehole coordinate system.

3.2 Determination of Collapse Pressure

Determination of collapse pressure is an important aspect for analysis related to the stability of borehole in hydrate reservoir. However, the maximum (σ_1) and minimum (σ_3) principle stresses around borehole are required if the Mohr–Coulomb criterion or its modified criterion is used for investigating borehole stability. The maximum and minimum

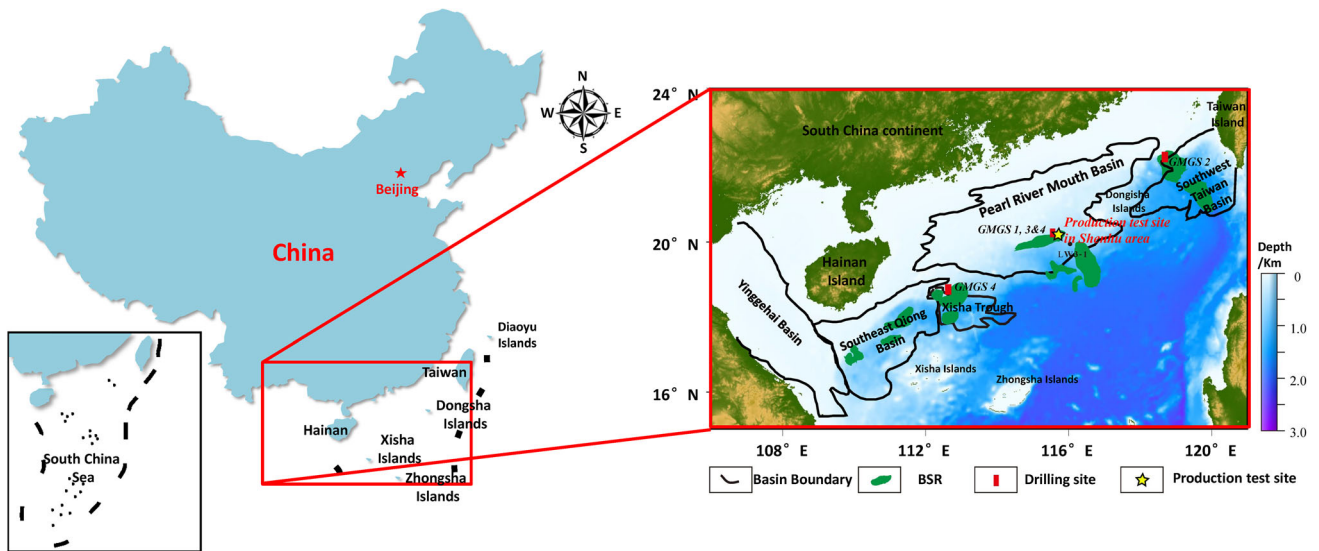


Fig. 2 Location (left) and geological map (right) of the study area (revised from Wu and Wang (2018))

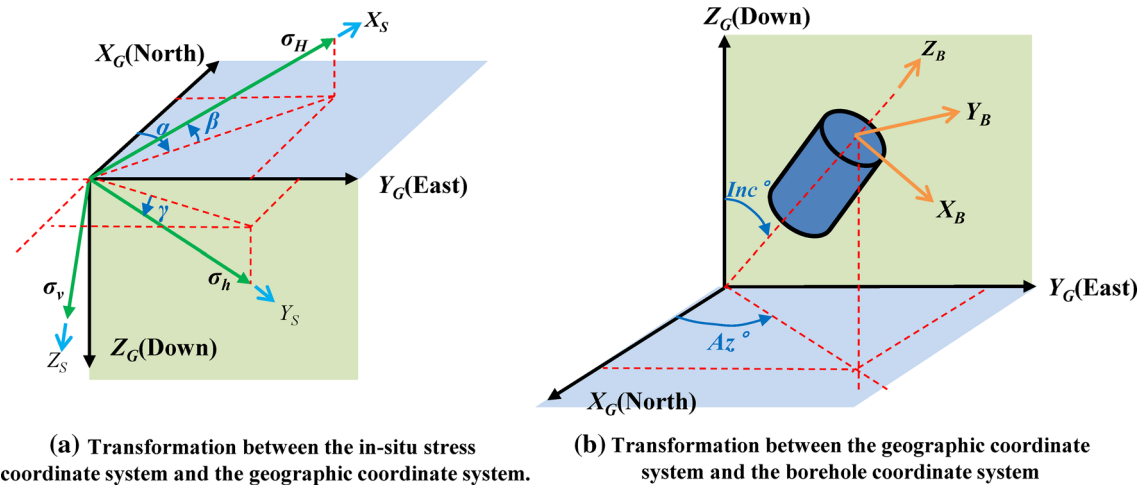


Fig. 3 Transformation of in situ stresses from the in situ stress coordinate system to the borehole coordinate system

principal stresses around wellbore can be obtained by Eqs. (5) and (6).

$$\begin{aligned} \sigma_i &= \sigma_r = P_m - P_p \\ \sigma_j &= 0.5(\sigma_\theta + \sigma_z) + 0.5\sqrt{(\sigma_\theta - \sigma_z)^2 + 4\sigma_{\theta z}^2} \\ \sigma_k &= 0.5(\sigma_\theta + \sigma_z) - 0.5\sqrt{(\sigma_\theta - \sigma_z)^2 + 4\sigma_{\theta z}^2} \end{aligned} \tag{5}$$

$$\begin{aligned} \sigma_1 &= \max(\sigma_i, \sigma_j, \sigma_k) \\ \sigma_3 &= \min(\sigma_i, \sigma_j, \sigma_k) \end{aligned} \tag{6}$$

The modified Mohr–Coulomb strength criterion (see Eq. 7) that suitable for the clayey silt hydrate reservoirs in

the northern South China Sea has been obtained by Li et al. [17].

$$\begin{aligned} \sigma_1 = \sigma_P &= \frac{2 \cos \varphi}{1 - \sin \varphi} C_0 + 12.02 \cdot S_h^{1.27} \\ &+ \frac{1 + \sin \varphi}{1 - \sin \varphi} \sigma_3 - 0.37\sigma_3^2 + 2.22\sigma_3 - 2.36 \end{aligned} \tag{7}$$

Later, the function $f(P_m)$ shown as Eq. (8) is defined to determine the collapse pressure of clayey silt hydrate reservoir:

$$\begin{aligned} f(P_m) &= \frac{2 \cos \varphi}{1 - \sin \varphi} C_1 + 12.02 \cdot S_h^{1.27} \\ &+ \frac{1 + \sin \varphi}{1 - \sin \varphi} \sigma_3 - 0.37\sigma_3^2 + 2.22\sigma_3 - 2.36 - \sigma_1 \end{aligned} \tag{8}$$

The drilling fluid pressure determined when $f(P_m)$ is equal to 0 is the collapse pressure, and the detailed determination method is provided in "Appendix 1".

3.3 Comprehensive Model of Reservoir Properties

Invasion of drilling fluid may result in hydrate dissociation during the drilling operation in hydrate reservoir and affect reservoir properties. Therefore, effect of drilling operation on hydrate dissociation around borehole needs to be investigated. The phase equilibrium equation of methane hydrate in seawater expressed by Eq. (9) [40] is used to judge the stability of hydrate.

$$P_{eq} = 9 \times 10^{-14} \times e^{0.1136T} \tag{9}$$

To our knowledge, effective stress is another factor affecting reservoir properties. In order to accurately describe the influence of hydrate saturation and effective stress on reservoir properties, the comprehensive model of hydrate reservoir properties has been proposed. Firstly, porosity of hydrate reservoir can be expressed as the following equation when hydrate dissociation and stress sensitivity are considered [41]:

$$\phi = \phi_0 \cdot (1 - S_h) \cdot (1.1039 \cdot \exp(-0.041\sigma)) \tag{10}$$

Similarly, permeability of hydrate reservoir during hydrate dissociation can be expressed as Eq. (11) with considering the stress sensitivity [41].

$$K = 7.5 \cdot (0.001\sigma^2 - 0.0572\sigma + 1.1267) \cdot (1 - S_h)^{7.9718} \tag{11}$$

The change in elastic modulus of hydrate reservoir during the drilling operation can be written as

$$E = E_0 \cdot (1 + 13.25 \cdot S_h) \cdot (-0.004\sigma^2 + 0.0242\sigma + 0.9784) \tag{12}$$

Poisson's ratio of hydrate reservoir was generally considered to be almost unchanged during hydrate dissociation [8]. However, the influence of effective stress on the Poisson's ratio of hydrate reservoir is revealed as Eq. (13) [41]:

$$v = v_0 \cdot (-0.0002\sigma^2 + 0.0139\sigma + 0.9697) \tag{13}$$

Cohesion and internal friction angle are both essential parameters for analyzing borehole deformation when the Mohr–Coulomb constitutive criterion is used. Just shown as

Eq. (14) and Eq. (15), the comprehensive modeling of these two parameters is expressed indirectly by other parameters

$$C = C_0 \cdot (1 - 1.2 \cdot (\phi - \phi_0)) \tag{14}$$

$$\varphi = 20 + 2.564 \cdot l_g \left[(59.83 - 1.785C)^2 + \sqrt{60.83 - 1.785C} \right] \tag{15}$$

The purpose of Eqs. (9)–(15) is to present the relationship between properties of hydrate-bearing sediments and hydrate saturation. However, the comprehensive model of hydrate-bearing sediment needs to be realized through secondary development during simulation of borehole stability in ABAQUS platform. In "Appendix 2", the codes of USD-FLD subroutine used to assess the comprehensive model of hydrate sediment are given.

3.4 Pressure Coefficient ς

In order to reveal the relationship between the bottom-hole pressure and the reservoir pressure, the pressure coefficient is defined as Eq. (16).

$$\varsigma = \frac{P_m}{P_p} \tag{16}$$

Therefore, the underbalanced and the overbalanced drilling operation corresponds to the conditions when the pressure coefficient is less and greater than 1.0, respectively.

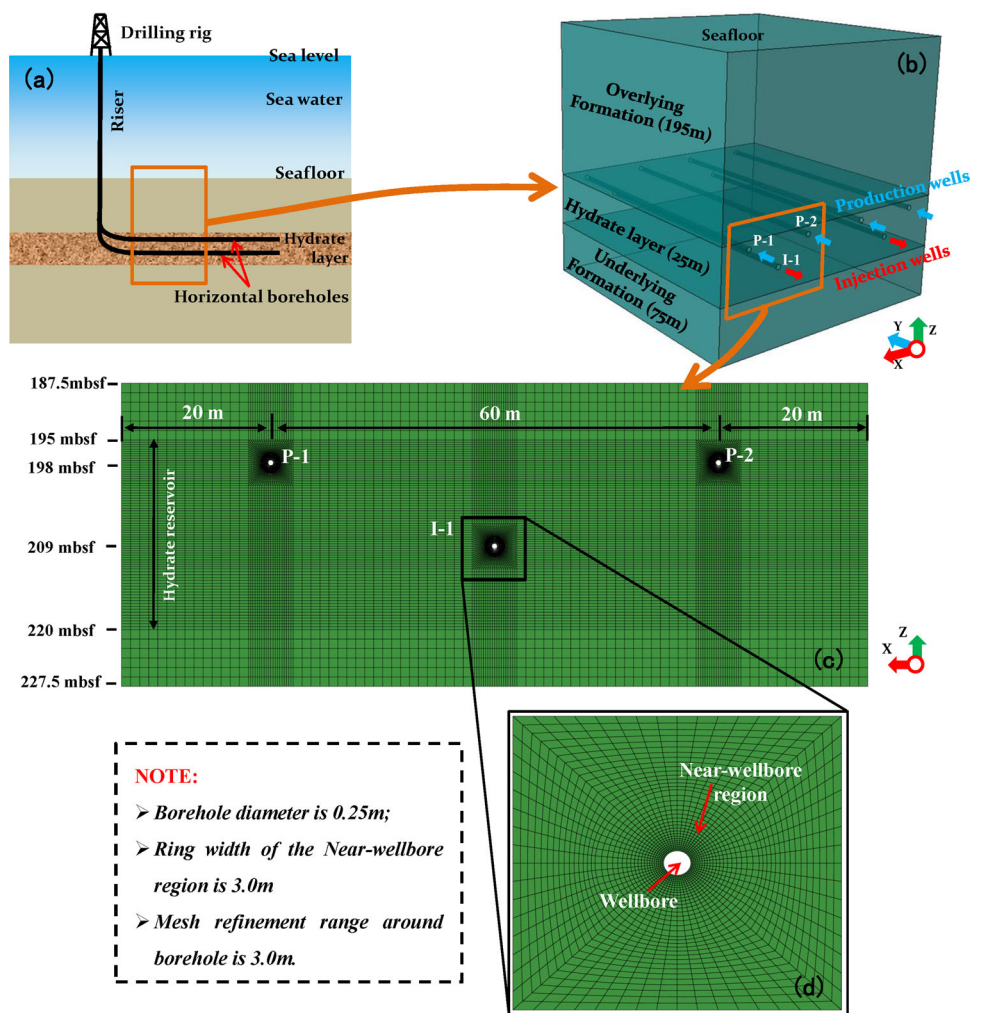
4 Numerical Modeling of the Simulation Model

Based on the fundamental theory above, simulation of borehole stability in hydrate reservoir can be conducted. In this section, finite element model for stability simulation of boreholes in horizontal well system was established. The development of finite element model in ABAQUS platform mainly includes: model configuration, simulation condition setting and mesh generation.

4.1 Model Configuration

Figure 4 displays the borehole trajectory of horizontal well system in hydrate reservoir and the finite element model. In Fig. 4a, two rows of horizontal wells are drilled parallel within hydrate reservoir. Among them, the boreholes in the upper row are used for methane production during the production stage, while the boreholes in the lower row are used for injection of thermal fluid. As mentioned in Fig. 4b and c, each well group consists of one injection well (I-1) and two production wells (P-1 and P-2). Although wells in the upper

Fig. 4 Configuration of the finite element model for numerically investigating of borehole stability during the drilling operation in hydrate-bearing sediment. **a:** 2D schematic of borehole configuration; **b** 3D schematic of borehole configuration in each well group; **c** mesh model for simulating the deformation of the boreholes and the strata due to hydrate dissociation; **d:** mesh refinement within the near-wellbore region



and lower rows play different roles in the production stage, respectively, three wells within one well group can be drilled simultaneously to shorten the drilling cycle. The investigation herein is aimed to analyze the deformation behavior of boreholes in one well group during the drilling operation.

At GMGS(2007)-SH2, an overlying formation with thickness of about 195 m exists between the hydrate reservoir and the seafloor, and the water depth is 1235 m [42]. According to exploration results, thickness of the hydrate reservoir at this site is about 25 m [33]. Of course, there are still infinite thicknesses of underlying formation below hydrate reservoir. Therefore, as mentioned in Fig. 4c, thicknesses of the overlying formation, hydrate reservoir and underlying formation are 7.5, 25 and 7.5 m, respectively. The horizontal distance between well P-1 and well P-2 is 60 m, and the vertical depth difference between the wells in the upper and the lower rows is 11 m. Besides, in order to improve production efficiency in the production stage, it is preferred to place the well that used for thermal fluid injection near the intermediate depth of hydrate reservoir. Notably, well I-1 is drilled at 11 m above

the bottom boundary of the hydrate reservoir in this study. Moreover, the axes of all wellbores are along the direction of the maximum horizontal principal stress, and mesh refinement has been carried out within the near-wellbore region (see Fig. 4d).

4.2 Initial Conditions

Borehole collapse in hydrate reservoir is a complex process involving seepage, borehole deformation and heat transfer. So, initial conditions of in situ stresses, pore pressure, porosity, both temperature and hydrate saturation need to be defined herein. It can be seen from Fig. 4 that thickness of the investigation model is as high as 40 m, so the longitudinal anisotropy must be taken into account. Figure 5 shows the reservoir properties at different depths of site GMGS(2007)-SH2. All original data in Fig. 5 were obtained from the public articles and plotted by Excel.

All initial conditions for investigation of borehole collapse in hydrate reservoir are as follows:

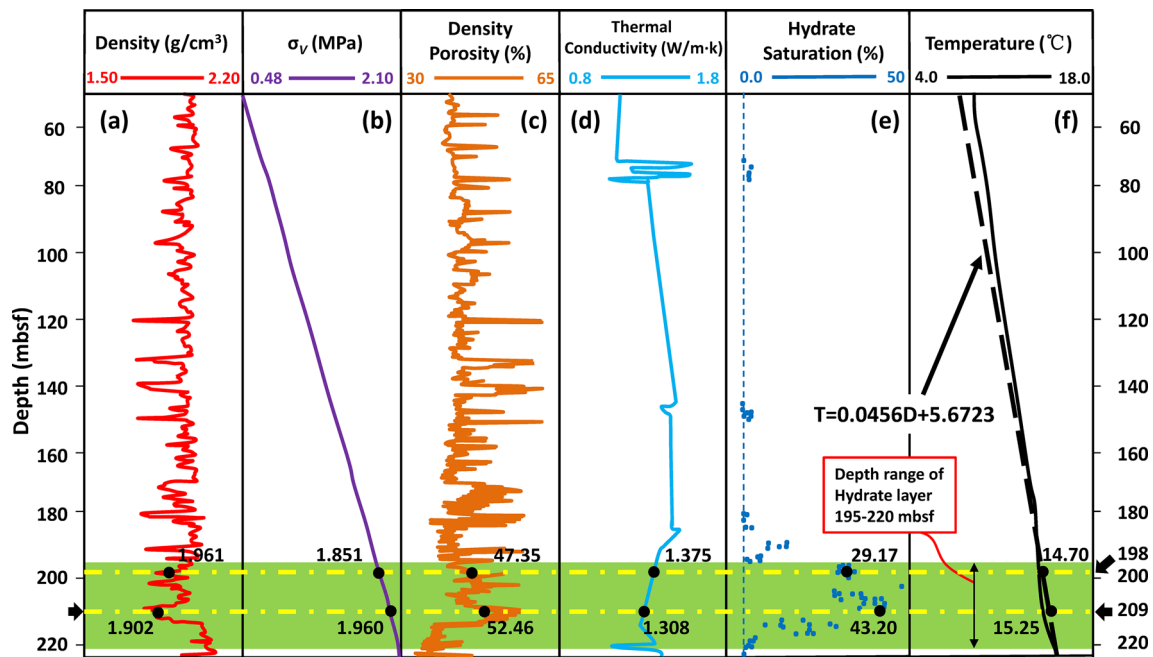


Fig. 5 Some logging data and stratigraphic characteristics at site GMGS (2007)-SH2 in Shenhu area, northern South China Sea. **a**: Density [33, 43–45]; **b**: effective vertical stress; **c**: density porosity [43–46]; **d**: thermal conductivity [47]; **e**: hydrate saturation [33, 46]; **f**: temperature [33, 43]

(1) Initial condition of stresses

In situ stresses at different depths of the investigation model herein can be obtained by Eq. (17) based on the density logging data shown in Fig. 5a.

$$\sigma_v = \int_{D=0}^{D=D} \rho \cdot g \cdot D$$

$$\sigma_H = \sigma_v \cdot \alpha_1$$

$$\sigma_h = \sigma_v \cdot \alpha_2$$
(17)

(2) Initial condition of pore pressure

Similar to the method for determining in situ stresses, the relationship between pore pressure and depth can be described as the following formula.

$$P_p = P_{atm} + \rho_{sea}g(H + D)$$
(18)

(3) Initial condition of temperature

The initial porosity within the model is defined according to Fig. 5c. In order to conveniently define the formation temperature, relationship between formation temperature and formation depth is fitted as Eq. (19) [33, 43]. In addition, the initial thermal conductivity is assumed to be 1.3W/(m-K) according to Fig. 5d.

$$T = 0.0456D + 5.673$$
(19)

(4) Initial condition of hydrate saturation

In addition, we can see from Fig. 5e that hydrate saturation is between 0 and 50% at site GMGS(2007)-SH2. In the present work, the piecewise function expressed as Eq. (20) is used to describe the longitudinal distribution of hydrate saturation in GMGS(2007)-SH2.

$$S_h(\%) = \begin{cases} 0 & (D \leq 195\text{mbsf}) \\ 2.346D - 422.74 & (195 \leq D \leq 209\text{mbsf}) \\ 571.07 - 2.596D & (209 \leq D \leq 220\text{mbsf}) \\ 0 & (D \geq 220\text{mbsf}) \end{cases}$$
(20)

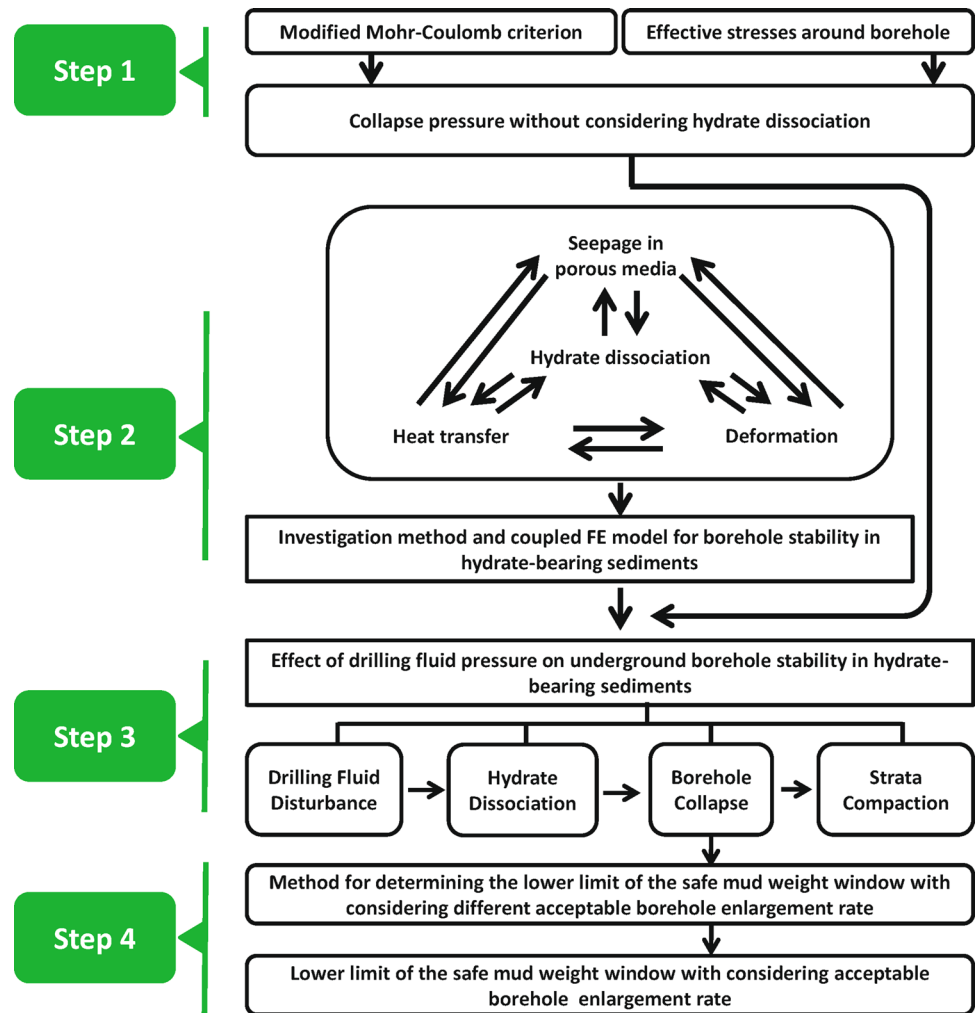
4.3 Loads and Boundary Conditions

Boundary conditions used during the investigation are as follows:

(1) Pore pressure and Temperature

During the whole simulation, both the temperature and pore pressure of borehole are always equal to those of drilling fluid. Temperature of drilling fluid within the injection well and the production well is 294.40K and 293.85K, respectively. However, pore pressure of drilling fluid within the injection well and the production well should be calculated by drilling mud density.

Fig. 6 Investigation workflow for analyzing borehole deformation during the drilling operation in hydrate-bearing sediments



(2) Displacement

The upper boundary of model is a free surface, and the normal displacements of other outer boundaries are 0.

(3) Loads

In addition, two loads, i.e., the overburden pressure applied to the upper boundary of the model and the bottom-hole pressure applied to the borehole, were also defined. Among them, the overburden pressure applied to the upper boundary of the model is 13.60MPa. However, the bottom-hole pressure applied to the borehole is positively correlated with the drilling fluid density and wellbore depth. In order to present investigation more systematically, Fig. 6 displays the workflow for conducting investigation on influence of drilling fluid pressure on the borehole deformation during the drilling operation in hydrate reservoir.

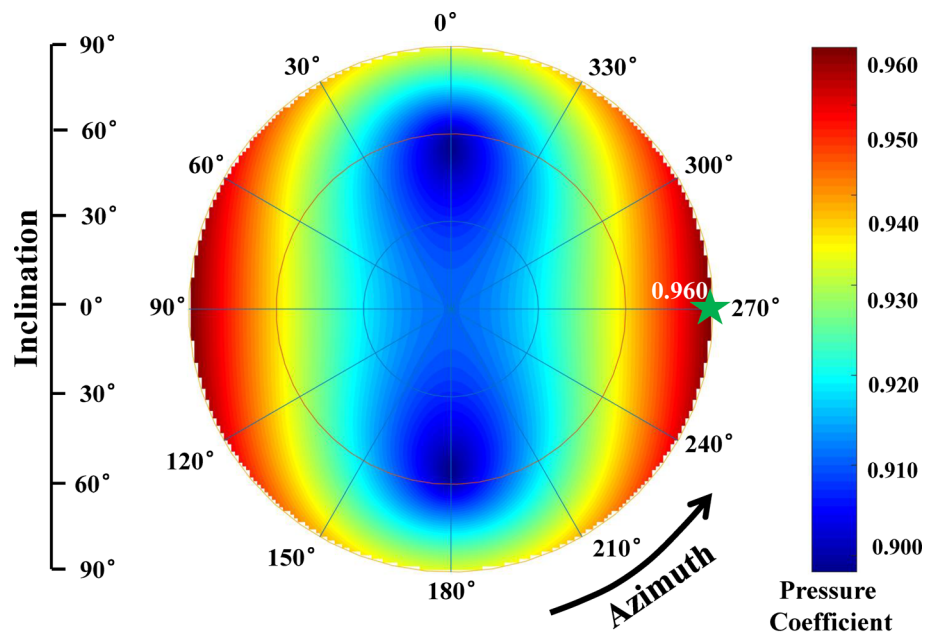
5 Results and Discussion

The drilling fluid formula used in the present work is: Water + 15% NaCl + 1% PVP(K90) + 0.9% CMC. In the present work, change of drilling fluid density is mainly realized by adding soil slurry. The drilling fluid used here only considers the rheology (viscosity, etc.) of the drilling fluid, and its hydrate inhibition has not been seriously considered.

5.1 Collapse Pressure Without Considering Hydrate Dissociation

The collapse pressure for all borehole trajectories at 209mbsf (meters below seafloor) of site GMGS(2007)-SH2 was obtained and is illustrated in Fig. 7. Henceforth, Fig. 7 is plotted by programming with MATLAB software, and all codes can be seen in Supplementary Material. The radial and axial coordinates in Fig. 7 represent the inclination angle and the azimuth angle, respectively, and each point in Fig. 7 represents a borehole trajectory. As a matter of fact, borehole

Fig. 7 The collapse pressure for different borehole trajectories at 209 mbsf of GMGS(2007)-SH2 determined by the modified Mohr–Coulomb strength criterion when hydrate dissociation is neglected



trajectory affects the effective stresses on borehole and collapse pressure of the hydrate reservoir. Therefore, collapse pressure at different points in Fig. 7 differs from each other. As can be seen in Fig. 7, the minimum collapse pressure (corresponding to a pressure coefficient of 0.900) occurs when the inclination angle of some boreholes is about 55 degrees. However, the maximum collapse pressure (corresponding to the maximum pressure coefficient of 0.960) displays on some horizontal boreholes, whose azimuth angles are 90 and 270 degrees, respectively.

In this work, the horizontal borehole with the azimuth angle of 270 degrees (the green pentagram in Fig. 7) is selected as the investigation object. We can see from Fig. 7 that the collapse pressure expressed by the pressure coefficient was 0.960 for this type of borehole trajectory. However, it is still unknown how to determine the minimum mud density that does not result in the uncontrollable borehole collapse caused by hydrate dissociation in hydrate reservoir. Therefore, a series of bottom-hole pressure represented by pressure coefficients between 0.96 and 1.05 are chosen for the subsequent simulation. If necessary, some new pressure coefficients can be properly inserted among those values.

5.2 Disturbance of Drilling Fluid to Hydrate Reservoir

Temperature and pore pressure within the hydrate reservoir are the two most important factors affecting the stability of natural gas hydrate. However, disturbance of drilling fluid may result in the hydrate dissociation, thus affecting borehole stability [48]. Evolution analysis of temperature and pore pressure within the near-wellbore region during the drilling

Table 1 Drilling parameters used for simulation

Parameter	Object	Value	Unit
Total drilling time, t	All boreholes	24	h
Rate of penetration, ROP		50	m/h
Length of horizontal section, L		1200	m
Temperature T	P-1 & P-2	293.85	K
	I-1	294.40	K
Pressure coefficient, ζ	All boreholes	0.98 ~ 1.15	–

operation is the prerequisite for investigating hydrate dissociation and the resulting borehole deformation. Table 1 shows the parameters used for simulating the disturbance of drilling fluid during the drilling operation in hydrate reservoirs.

In order to clearly understand the effect of drilling fluid to reservoir temperature during the drilling operation in hydrate reservoir, Fig. 8 illustrates evolution of the temperature front within the near-wellbore region during the whole drilling operation. In Fig. 8, the evolution curve of temperature disturbance front was obtained by determining the position of the disturbance front at different drilling time. Then, the advancement rate of temperature disturbance front around wellbore V_t can be calculated by Eq. (21).

$$V_t = \frac{DT_2 - DT_1}{t_2 - t_1} \tag{21}$$

As shown in Fig. 8, for all boreholes within the investigation model, the temperature front gradually advances forward due to the disturbance of the drilling fluid. Although subtle difference exists in reservoir temperature at depths of the boreholes in the upper (well P-1 and P-2) and lower

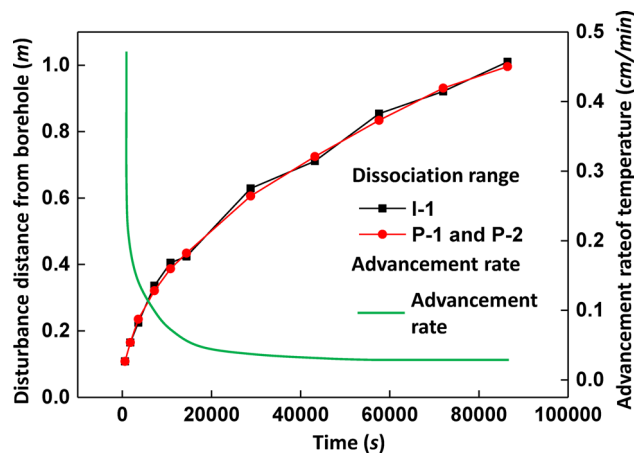


Fig. 8 Evolution of temperature front in the near-wellbore region during the drilling operation in hydrate reservoir

(well I-1) rows, the evolution of temperature front during the entire drilling operation is similar to each other. At the end of the drilling operation, the distances between the final temperature front and the boreholes are all approximately 1.000 m. In addition, the gradually decreasing slope of the temperature front curves in Fig. 8 implies the fact that the advancement rate of the temperature front decreases with the drilling operation, and the advancement rate curve of temperature front in Fig. 8 can also confirm this. At the beginning of the drilling operation, the advancement rate of temperature front was 0.476 cm/min. However, after the drilling operation lasted for 17 h, the advancement rate of temperature front was basically maintained at 0.025 cm/min. It is due to the fact that dissociation of natural gas hydrates in the near-wellbore region absorbs a large amount of heat, resulting in decline of heat transfer in hydrate reservoir near the temperature front.

Figure 9 displays the effect of bottom-hole pressure on pore pressure within the whole model when the pressure coefficient is 0.98. As illustrated in Fig. 9, at the beginning of the drilling operation, the invasion of drilling fluid mainly occurs in the near-wellbore region. As the drilling operation continues, the invasion front of drilling fluid gradually moves away from all boreholes in the finite element model. When the drilling operation lasts for 1800s (i.e., half an hour), the pore pressure disturbance ranges around the injection well and production well are 10.235 m and 12.362 m, respectively. Nearly the whole hydrate reservoir was disturbed by the invasion of drilling operation after drilling in hydrate reservoir for about 8 h. Furthermore, pore pressure distribution around boreholes at different depths differs from each other significantly in the same moment, which may lead to the difference in hydrate dissociation within the near-wellbore region around different wellbores. From Fig. 8 and Fig. 9, it can also be clearly

found that effect of drilling fluid invasion in hydrate-bearing sediments is severer on pore pressure as compared to temperature.

5.3 Hydrate Dissociation Around Wellbores

Hydrate dissociation is an important factor affecting borehole deformation while drilling through hydrate reservoirs [40]. And, difference in hydrate dissociation caused by invasion of drilling fluid mainly depends on the temperature and pressure of drilling fluid. However, only the effects of drilling fluid pressure (i.e., the bottom-hole pressure) on hydrate dissociation and borehole deformation within the near-wellbore region have been investigated in this paper, and the temperature of drilling fluid was considered to be same in all cases. Figure 10 displays the dissociation of natural gas hydrates within the near-wellbore region around three boreholes within the model under different bottom-hole pressure. Investigation results around the two production wells should be similar to each other due to the symmetry of the model; thus, the results of both production wells are replaced with that of well P-1.

For one thing, as observed from Fig. 10, the range of hydrate dissociation around different wellbores differs significantly due to the differences in temperature and pore pressure around different wellbores. The range of hydrate dissociation around wellbores in the upper row is evidently smaller than that around well I-1 when the same pressure coefficient is applied to all these three wellbores. It can be seen from Fig. 10b that methane hydrates in an annular area with a range of about 30.522 cm around well I-1 have dissociated at the end of the drilling operation when the pressure coefficient is 0.98. However, hydrate dissociation occurs only within a range of about 25.124 cm around wellbores in the upper row for the same conditions (see Fig. 10a). Difference in range of hydrate dissociation around different wellbore can be attributed to the disturbance of drilling fluid to hydrate reservoir around the wellbore. More specifically, this difference is almost entirely due to the difference in the values of drilling fluid density and pore pressure around different wellbore (see Figs. 8 and 9).

For another, effect of bottom-hole pressure on hydrate dissociation around three different wellbore in the model is similar to each other. As can be seen from Fig. 10, for all three wellbore in the investigation model, dissociation of methane hydrates within the near-wellbore region gradually slows down as the bottom-hole pressure increases. The final range of hydrate dissociation around wellbore in the upper row decreased from 25.121 to 20.544 cm when the pressure coefficient was increased from 0.98 to 1.04, with a reduction of 18.23%. However, for the injection well in the lower row (i.e., well I-1), the final range of hydrate dissociation has decreased from 31.113 to 24.550 cm under the same

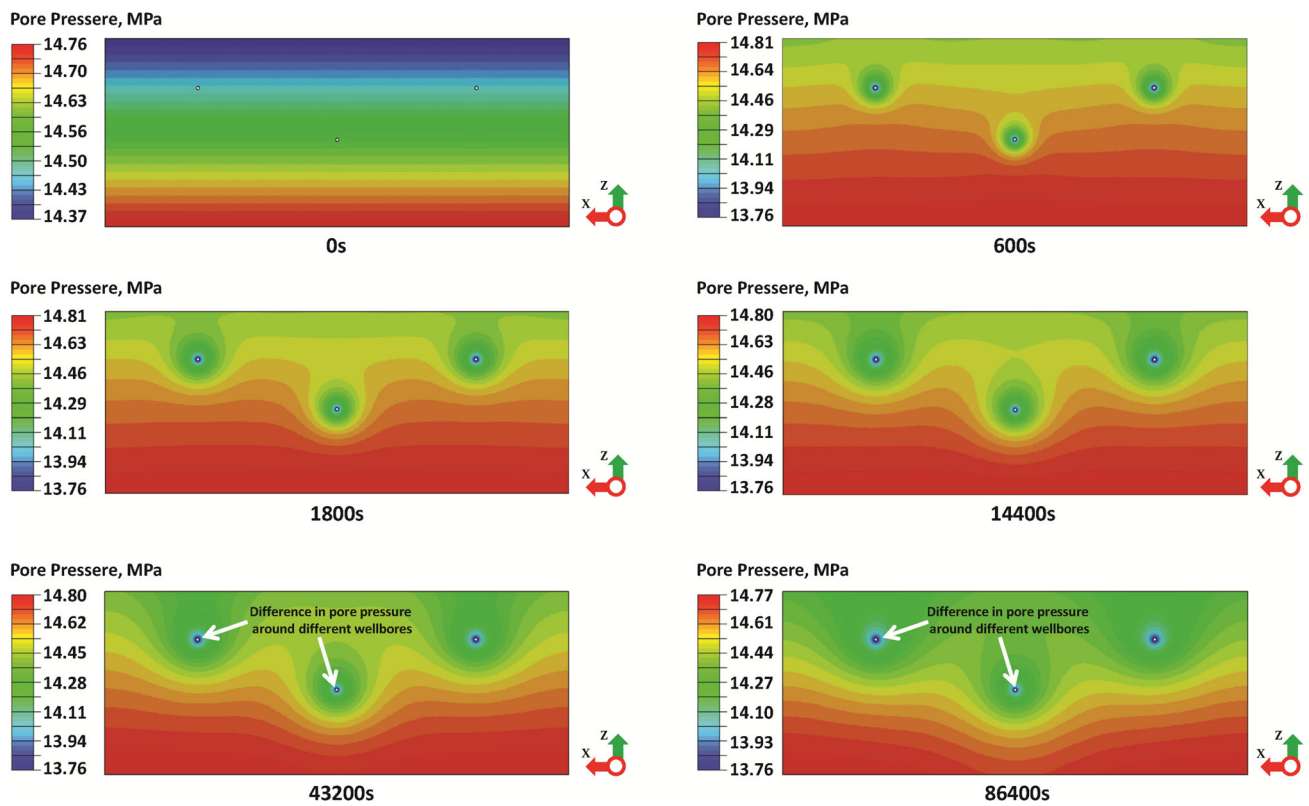


Fig. 9 Evolution of reservoir pore pressure disturbed by the drilling operation in hydrate reservoir when the pressure coefficient is 0.98

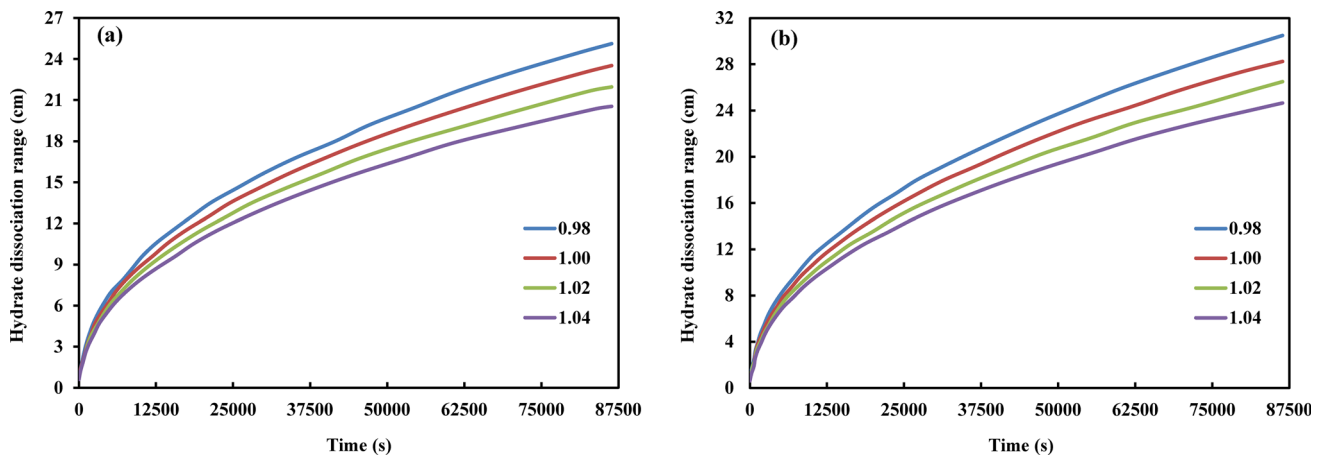


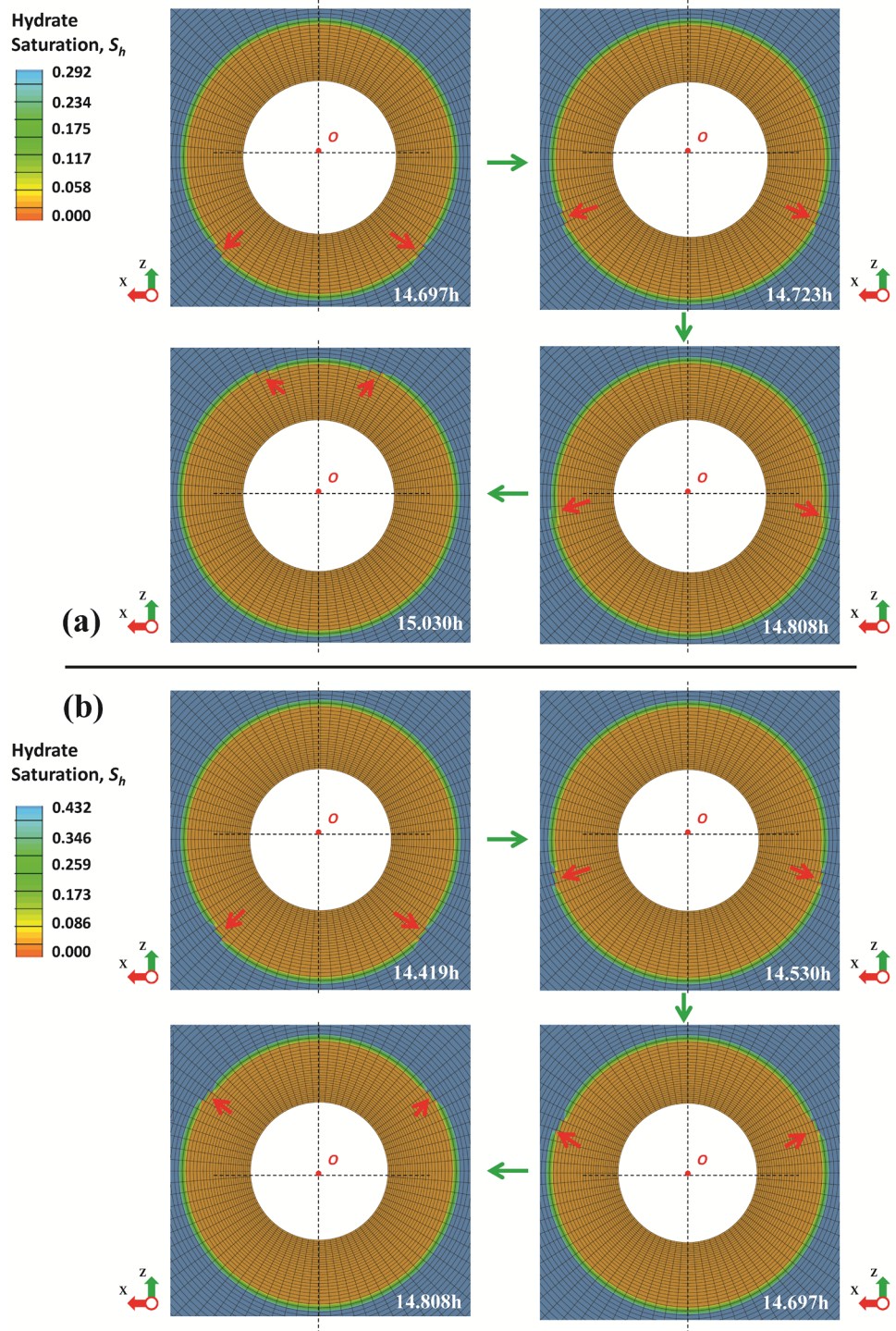
Fig. 10 Radial evolution of dissociation range around different wellbore when the bottom-hole pressure is different. a: Dissociation range of natural gas hydrate for two production wells in the upper row (well P-1 and P-2); b: dissociation range of natural gas hydrate for well I-1 in the lower row

conditions. The phase equilibrium conditions of natural gas hydrate may be helpful to explain this. Furthermore, properties of the drilling fluid (mainly the salinity, temperature and pressure) within wellbore in the lower row are more likely to destabilize the natural gas hydrates. Although natural gas hydrate is stable in hydrate reservoir under natural conditions, the methane hydrate around the wellbore is more likely to be in conditions of instability under low bottom-hole pressure. The invasion of drilling fluid into hydrate reservoir becomes

more dominant as the bottom-hole pressure increases, resulting in an increase in the pore pressure of the near-well zone, which may inhibit the hydrate dissociation to some extent.

It is generally believed that natural gas hydrates in the reservoir at the same distance from borehole show dissociation simultaneously during the drilling operation, but the fact is not so ideal. Figure 11 shows the circumferential evolution of hydrate dissociation around all horizontal wellbore during the drilling operation. Figure 11 reveals that hydrate disso-

Fig. 11 Circumferential evolution of hydrate dissociation circle when the pressure coefficient is 0.98. **a:** wells in the upper row (well P-1 and P-2); **b:** well I-1 in the lower row



ciation firstly appears at the bottom of the dissociation circle and gradually extends circumferentially toward the top of the dissociation circle. When the drilling operation has lasted for about 14.500 h, the complete circumferential evolution of one dissociation circle around wellbore in the upper and lower rows required approximately 0.895 and 0.783 h, respectively; time difference is 0.112 h. The circumferential evolution of

hydrate dissociation circle around horizontal wellbore can be attributed to the vertical anisotropy of reservoir characteristics. Reservoir temperature at the bottom of the horizontal wellbore is generally higher, due to which gas hydrates near the bottom of the wellbore may dissociate more easily.

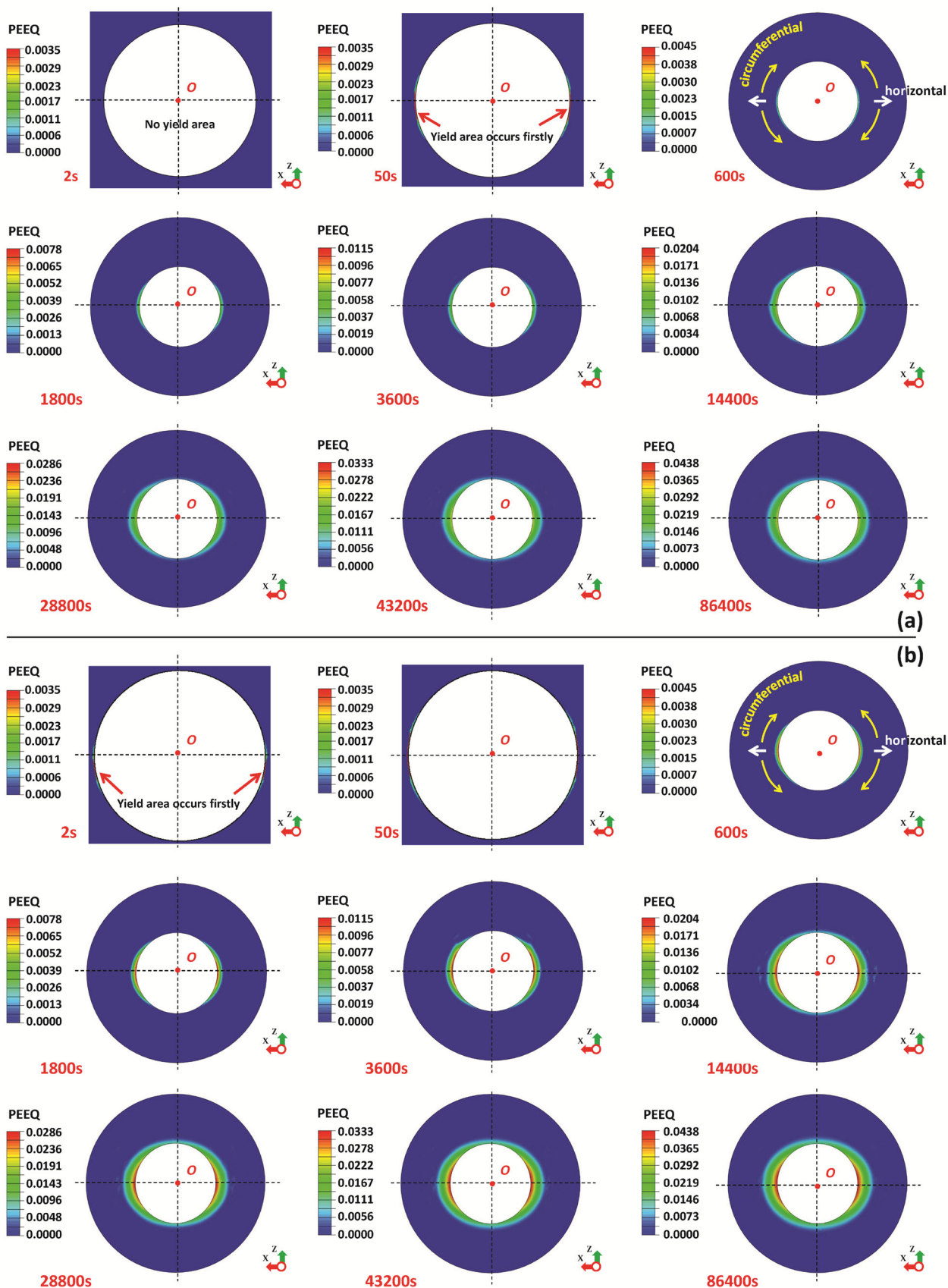
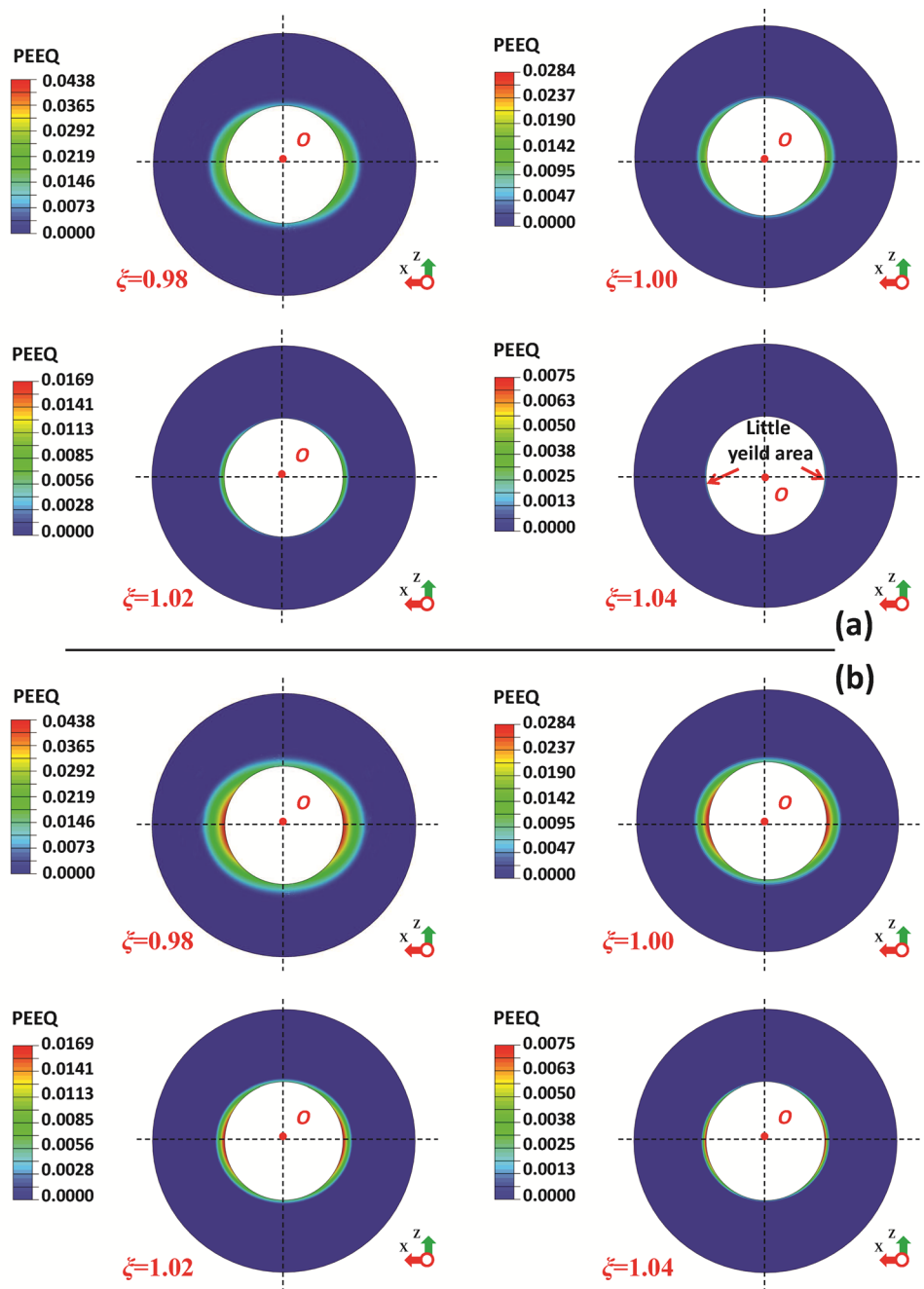


Fig. 12 Evolution of collapse area (equivalent plastic strain, i.e., PEEQ herein) around borehole within the near-wellbore region throughout the whole drilling operation when the pressure coefficient is 0.98. a: well P-1 and P-2; b: well I-1

Fig. 13 a: Final equivalent plastic strain within the near-wellbore region for well P-1 and P-2 when the pressure coefficient is different; **b:** final equivalent plastic strain within the near-wellbore region for well I-1 when the pressure coefficient is different



5.4 Deformation Behavior of Boreholes

Dissociation of natural gas hydrates within the near-wellbore region is bound to cause the decrease of reservoir strength and the possible borehole collapse [16, 25]. Considering the fact that borehole collapse may occur in any area around borehole where the equivalent plastic strain appears, Fig. 12 displays the evolution of collapse area around each wellbore throughout the drilling operation when the pressure coefficient is 0.98. As shown in Fig. 12, borehole collapse initially occurs at two points on borehole, which are located below the

intersections of the horizontal plane containing the wellbore axis and another plane perpendicular to wellbore axis. For injection well and production well, distances between initial collapse point and horizontal plane containing the wellbore axis are 1.849 cm and 1.532 cm, respectively. Besides, the initial collapse area around the wellbore in the lower row appears earlier than that around the wellbore in the upper row at the beginning of the drilling operation. The occurrence time of initial collapse points around the injection well is 2.00 s, but the initial collapse points did not appear around the production well until the drilling operation lasted 50.00 s.

This is mainly due to the fact that the higher reservoir temperature around the wellbore in the lower row makes dissociation of natural gas hydrates more prone to occur. In the subsequent drilling operation, the collapse area not only expands horizontally, but also circumferentially along the borehole from both the initial collapse points. Although both the horizontal and circumferential expansion of the collapse area around wellbore is occurring simultaneously throughout the whole drilling operation, there is difference in the time intervals during which each type of expansion dominates. The circumferential expansion of the collapse area occurs primarily at the beginning of the drilling operation, during which its horizontal expansion is not particularly evident. The circumferential expansion basically stops when the circumferential expansion of the collapse area makes it closed around the wellbore, while its horizontal expansion becomes more and more apparent. The time required for the collapse area to close around the injection well and the production well is 4.00 h and 8.00 h, respectively. At the end of the drilling operation, elliptical collapse areas with different sizes are formed around wellbore, and the long axes of these elliptical collapse areas are along the direction of the minimum horizontal stress.

Figure 13 illustrates effect of bottom-hole pressure on borehole collapse during the drilling operation in hydrate reservoir. It can be seen from Fig. 13 that although evolution of collapse areas around wellbore in the upper row is slightly different from that which is around wellbore in the lower row, the influence of bottom-hole pressure on the final collapse area is also similar. Indeed, borehole collapse is remarkable when the bottom-hole pressure is relatively low due to the severe hydrate dissociation, which is detrimental to maintaining wellbore integrity. When the drilling fluid density is 0.98, final collapse area around the injection well is 0.0211m², but final collapse area around the production well is only 0.0128m², whereas not only hydrate dissociation around wellbore, but also borehole collapse will be effectively suppressed with the increase of bottom-hole pressure. When the drilling fluid density becomes 1.04, final collapse area around the injection well is reduced to 0.0034m², and final collapse area around the production well is also reduced to an almost negligible value of 0.0010m². Therefore, overbalanced drilling technology is recommended for the drilling operation in hydrate reservoirs, but attention should be paid to avoid the hydraulically induced fractures within the near-wellbore region caused by the excessive bottom-hole pressure.

Borehole collapse during the drilling operation in hydrate reservoir can be represented by the schematic diagram shown in Fig. 14. In order to facilitate the description of collapse area around the wellbore, the borehole enlargement rate ε is defined by the following equation.

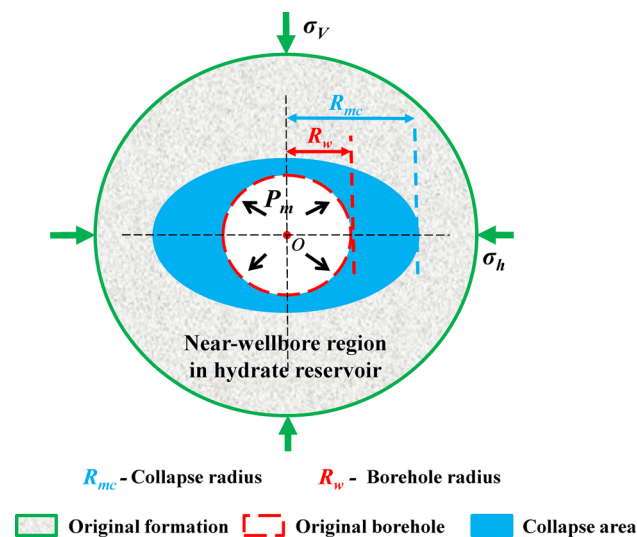


Fig. 14 Schematic diagram borehole collapse in hydrate-bearing sediments for all drilling cases

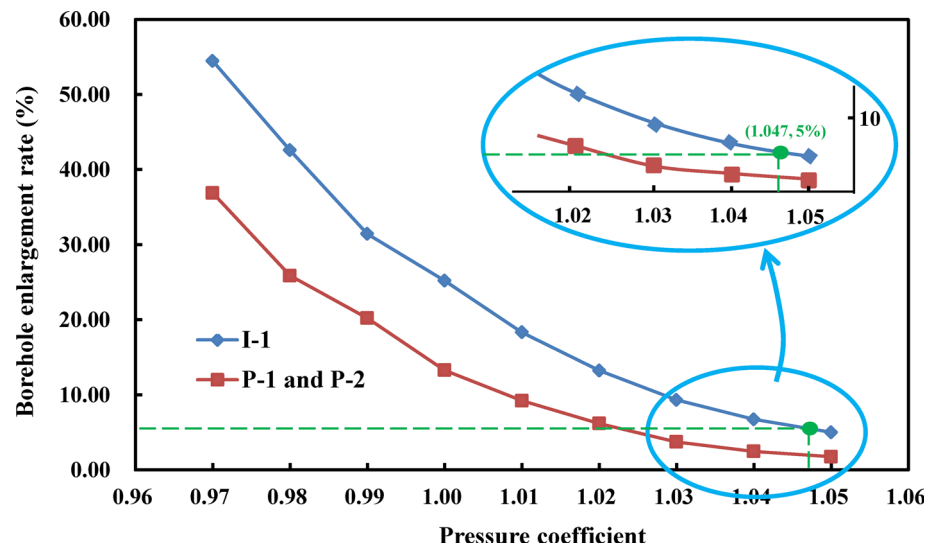
$$\varepsilon = \frac{R_{mc} - R_w}{R_w} \times 100\% \tag{22}$$

All parameters used in Eq. (22) are illustrated in Fig. 14. The larger borehole enlargement rate illustrates more serious borehole collapse. For example, if the borehole enlargement rate is 50%, that defines that the long axis of the elliptical collapse area is 0.5 m.

5.5 The Lower Limit of the Safe Mud Weight Window

Although the absence of borehole collapse during the drilling operations is a goal that all petroleum engineers have been pursuing, it is almost impossible for hydrate reservoirs. Therefore, the controllable borehole collapse is permitted while drilling through hydrate reservoir. In Fig. 13, the conclusion that collapse area around the wellbore decreases with the increase in bottom-hole pressure can only be qualitatively drawn when borehole instability cannot be quantitatively evaluated. However, the effect of bottom-hole pressure on borehole collapse can be quantitatively described with the aid of the borehole enlargement rate. Figure 15 shows the effect of bottom-hole pressure on borehole enlargement rate of different wells in the upper and lower rows within the finite element model. As can be seen from Fig. 15, borehole collapse area dramatically and nonlinearly diminishes with the increase of bottom-hole pressure. Relatively, effect of bottom-hole pressure on the borehole collapse is highly dominant in the lower range of bottom-hole pressure. Almost no collapse area displays around any wellbore when the pressure coefficient reaches 1.06, and the borehole enlargement rate of wellbore in the upper and lower rows is only 0.92% and 2.25%, respectively. Moreover, borehole enlargement rate of

Fig. 15 Relationship between the borehole enlargement rate and the pressure coefficient



two wells in the upper row (well P-1 and P-2) is all lower than that of the well in the lower row (well I-1) at any drilling time, which is consistent with the results depicted in Figs. 12 and 13.

Based on this, the lower limit of the safe mud weight window with considering different acceptable borehole enlargement rate can be determined. The determination method is illustrated in Fig. 15: The pressure coefficient of well I-1 within the model under certain borehole enlargement rate is defined as the lower limit of the safe mud weight window in this work. The mud density determined with the method shown in Fig. 15 can ensure that the borehole enlargement rate of all wells is less than or equal to the acceptable borehole enlargement rate. Figure 16 shows the lower limit of the safe mud weight window when different acceptable borehole enlargement rate is considered. Additionally, it can be seen from Fig. 16 that higher the requirement for wellbore integrity in hydrate reservoir is, higher will be the lower limit of the safe mud weight window. Conversely, if the requirement for wellbore integrity is not so strict, the lower limit of the safe mud weight window can be appropriately reduced. For example, if the upper limit of the acceptable borehole enlargement rate is 5.0%, the pressure coefficient should be larger than 1.047, whereas the lower limit of the safe mud weight window is 1.016 if the acceptable borehole enlargement rate is limited to 15%. In this way, determining the lower limit of the safe mud weight window based on the collapse pressure in 5.1 may result in fatal borehole damage. The study in this section can provide support for avoiding wellbore instability in drilling engineering of hydrate reservoirs, which is the ultimate goal of this study.

For error analysis, two numerical simulations of borehole stability in hydrate reservoir under the same conditions were repeated, and two other sets of results of the lower limit of safe mud weight window under different acceptable bore-

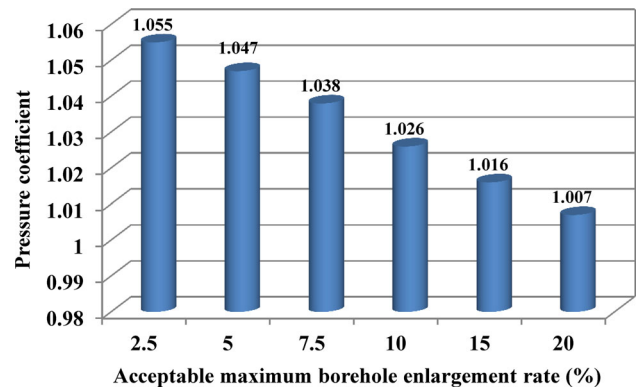


Fig. 16 The lower limit of the safe mud weight window in hydrate-bearing sediments with considering different acceptable borehole enlargement rate

hole enlargement rates were obtained. The results of error analysis are shown in Table 2. As it can be observed from Table 2, the standard deviation of designed mud density is 0.00400, 0.00265, 0.00503, 0.00361, 0.00404 and 0.00500 when acceptable borehole enlargement rate is 2.5%, 5.0%, 7.5%, 10.0%, 15.0 and 20.0%, respectively. The maximum standard deviation is 0.00503, which is enough to show the dispersion of the results obtained from the three simulations is minor. In addition, from Table 2, it can be seen that the maximum standard error is only 0.00291. By analyzing this reason, the errors of all simulation results may be caused by human factors, such as human data acquisition or meshing operation.

5.6 Reservoir Compaction and Stratum Deformation

Hydrate dissociation within the near-wellbore region during the drilling operation will necessarily affect the stratum stability to some extent. Figure 17 illustrates the stratum

Table 2 Error analysis

$\varepsilon/\%$	Designed mud density	Average value	Standard deviation	Standard error	95% confidence interval	
					Lower limit	Upper limit
2.5	1.055	1.0550	0.00400	0.00231	1.0451	1.0649
	1.051					
	1.059					
5.0	1.047	1.0460	0.00265	0.00153	1.0394	1.0526
	1.043					
	1.048					
7.5	1.038	1.0373	0.00503	0.00291	1.0248	1.0498
	1.032					
	1.042					
10.0	1.026	1.0270	0.00361	0.00208	1.0180	1.0360
	1.031					
	1.024					
15.0	1.016	1.0153	0.00404	0.00233	1.0053	1.0254
	1.011					
	1.019					
20.0	1.007	1.0070	0.00500	0.00289	0.9946	1.0194
	1.002					
	1.012					

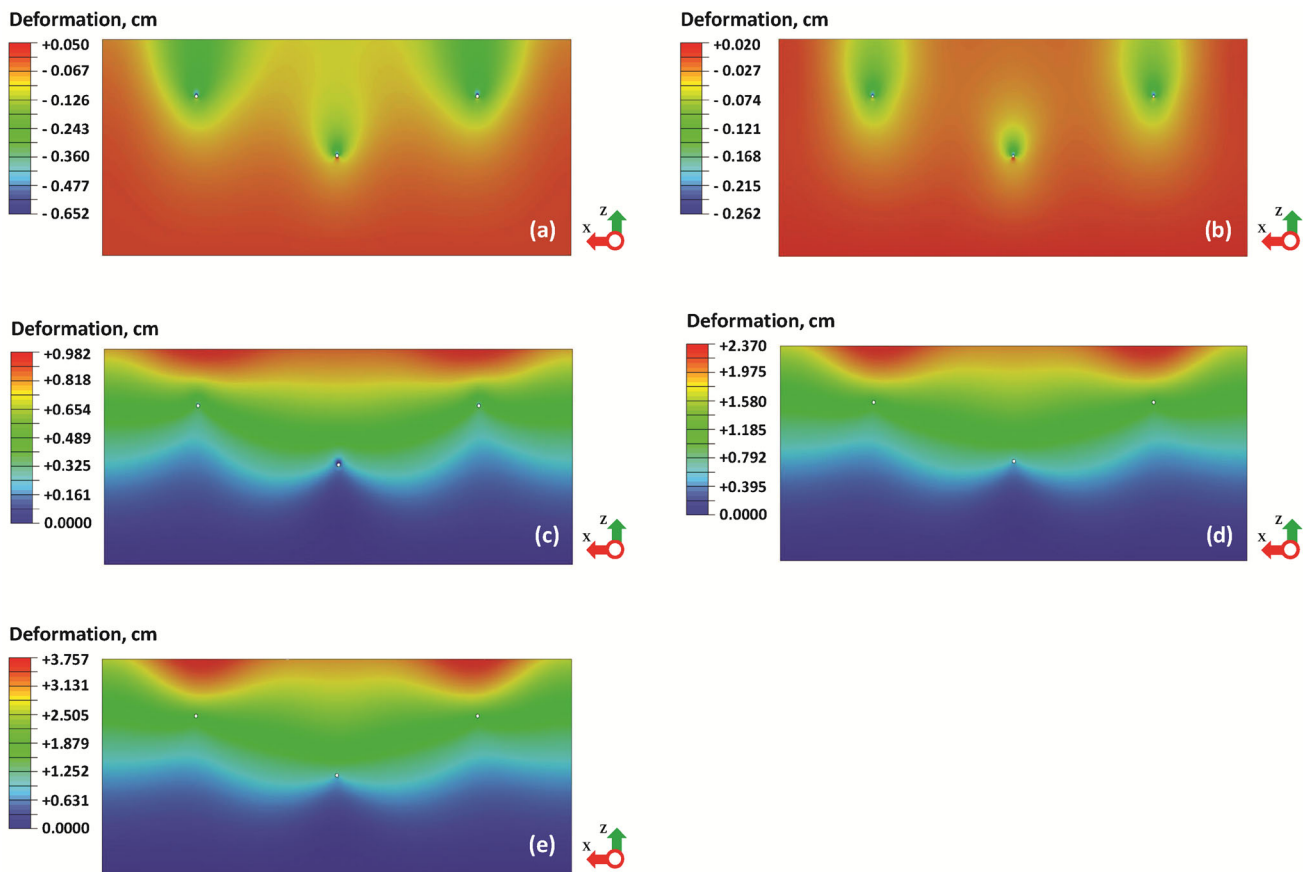


Fig. 17 The strata deformation within the simulation model during the drilling operation in hydrate-bearing sediments when the pressure coefficient is different. **a:** $\xi = 0.97$; **b:** $\xi = 0.99$; **c:** $\xi = 1.01$; **d:** $\xi = 1.03$; **e:** $\xi = 1.05$

deformation within the whole model caused by both the drilling operation and the hydrate dissociation under different bottom-hole pressures. The negative and positive values in Fig. 17 represent the subsidence and the uplift of stratum, respectively. It can be seen from Fig. 17 that the drilling operation in hydrate reservoir has little effect on stratum deformation, which are all within 4.00 cm. Nevertheless, some conclusions still can be drawn from simulation results.

As shown in Fig. 17a, if the under-balanced drilling technology was adopted, reservoir fluids around wellbore are pumped out in large quantities, resulting in both the reduction of pore pressure and the increase of effective stresses within the near-wellbore region. The formation near the wellbore is compacted due to the extraction of reservoir fluids, and the maximum deformation occurs at the borehole. It can also be seen from Fig. 17a the maximum deformation is just 0.652 cm, which occurs at the highest position of borehole. The concrete manifestation is that the stratum above wellbore has obvious subsidence, while the stratum below wellbore has a general uplift. Despite this factor, some differences in stratum deformation around different wellbore may still be presented. Comparatively, the deformation of boreholes in the upper row within the model has a greater influence on the stability of the stratum nearby.

However, the stratum deformation caused by hydrate dissociation in overbalanced drilling operation is significantly different from that caused by hydrate dissociation in underbalanced drilling operation (see Fig. 17). When the overbalanced drilling operation was carried out, invasion of drilling fluid into the reservoir caused increase of pore pressure and increased the stratum porosity to a certain extent. Although hydrate dissociation can cause the compaction of hydrate reservoir, the expansion of pores in stratum not only offsets this compaction, but even causes the reverse deformation in the opposite direction of compaction. It can be seen from Fig. 17b to e that the maximum stratum deformation occurs at the upper boundary of the model, more specifically the upper boundary of the model above the two wellbores in the upper row. Moreover, the deformations of all nodes in the model increase with the increase of the bottom-hole pressure. When the pressure coefficient is 0.99, the maximum deformation is 0.982 cm, but it has increased to 3.757 cm if the pressure coefficient becomes 1.28. Therefore, reservoir deformation can be neglected during the drilling operation in hydrate reservoir. However, the deformation of reservoir may be surprising in the production stage and needs to be considered.

6 Conclusion and Future Work

The main concluding points are mentioned below:

- (1) While drilling through hydrate reservoir, drilling operation affects the pore pressure more seriously as compared to reservoir temperature. Moreover, at the end of drilling operation, the temperature of the annular region with a width of about 1.0 m was deviated, and the pore pressure is affected throughout the model.
- (2) Dissociation range of gas hydrates around wells in the lower row (injection wells) is always larger than the range of the upper row (production wells). In addition, hydrate dissociation around all wellbores will gradually decrease with the increase of bottom-hole pressure.
- (3) Borehole collapse occurs around all boreholes in horizontal well system during the drilling operation. It is just that borehole collapse around wells in the upper row (injection wells) is always weaker than that around the well in the lower row (production wells).
- (4) The lower limit of the safe mud weight window increases gradually with the improvement of borehole stability limits while drilling through hydrate reservoir with horizontal well system.

7 Appendix 1. Determination of $f(P_m)$ and Newton–Raphson iterations for three different cases

The purpose of "Appendix 1" is to provide the method for determining the collapse pressure under complex stress conditions. In view of the difficulty in determining the relationship between the three effective principal stresses (σ_i , σ_j and σ_k), all the following three cases should be investigated:

- (1) When σ_r is the minimum effective principal stress, and σ_j is the maximum effective principal stress, the following equation can be obtained:

$$\begin{aligned}\sigma_1 &= 0.5(\sigma_\theta + \sigma_z) + 0.5\sqrt{(\sigma_\theta - \sigma_z)^2 + 4\sigma_{\theta z}^2} \\ \sigma_3 &= P_m - P_p\end{aligned}\quad (23)$$

Combining Eqs. (1) and (23) together gives the function $f(P_m)$:

$$\begin{aligned}f(P_m) &= E - F \cdot P_p + (F+1) \cdot P_m \\ &\quad - 0.74(P_m - P_p)^2 - A - \sqrt{(B - P_m)^2 + D}\end{aligned}\quad (24)$$

And, its first derivative is:

$$f'(P_m) = (F+1) - 1.48(P_m - P_p) + \frac{B - P_m}{\sqrt{(B - P_m)^2 + D}}\quad (25)$$

where A, B, C, D, E and F in Eq. (25) can be expressed as

$$\begin{aligned}
 A &= \sigma_B^{xx} + \sigma_B^{yy} - 2(\sigma_B^{xx} - \sigma_B^{yy})\cos 2\theta - 4\sigma_B^{xy}\sin 2\theta - P_p + \sigma_z \\
 B &= \sigma_B^{xx} + \sigma_B^{yy} - 2(\sigma_B^{xx} - \sigma_B^{yy})\cos 2\theta - 4\sigma_B^{xy}\sin 2\theta - P_p - \sigma_z \\
 D &= 4\sigma_{\theta z}^2 \\
 E &= \frac{4\cos\varphi}{1 - \sin\varphi}C_0 + 24.04S_h^{1.27} - 4.72 \\
 F &= \frac{2(1 + \sin\varphi)}{1 - \sin\varphi} + 4.44
 \end{aligned}
 \tag{26}$$

- (2) When the stress σ_r is the intermediate principal stress, and σ_j is the maximum effective principal stress, the following equation can be obtained:

$$\begin{aligned}
 \sigma_1 &= 0.5(\sigma_\theta + \sigma_z) + 0.5\sqrt{(\sigma_\theta - \sigma_z)^2 + 4\sigma_{\theta z}^2} \\
 \sigma_3 &= 0.5(\sigma_\theta + \sigma_z) - 0.5\sqrt{(\sigma_\theta - \sigma_z)^2 + 4\sigma_{\theta z}^2}
 \end{aligned}
 \tag{27}$$

The function $f(P_m)$ in this case can be expressed by combining Eqs. (1) and (27)

$$\begin{aligned}
 f(P_m) &= E + (0.5F - 1)(A - P_m) \\
 &\quad - (0.5F + 1)\sqrt{(B - P_m)^2 + D} \\
 &\quad - 0.185\left[(A - P_m) - \sqrt{(B - P_m)^2 + D} \right]
 \end{aligned}
 \tag{28}$$

The first derivative is

$$\begin{aligned}
 f'(P_m) &= (1 - 0.5F) + (0.5F + 1)\frac{(B - P_m)}{\sqrt{(B - P_m)^2 + D}} \\
 &\quad - 0.185\left[\frac{(B - P_m)}{\sqrt{(B - P_m)^2 + D}} - 1 \right]
 \end{aligned}
 \tag{29}$$

- (3) The following equation can be obtained when σ_r is the maximum effective principal stress, and σ_j is the minimum effective principal stress:

$$\begin{aligned}
 \sigma_1 &= P_m - P_p \\
 \sigma_3 &= 0.5(\sigma_\theta + \sigma_z) - 0.5\sqrt{(\sigma_\theta - \sigma_z)^2 + 4\sigma_{\theta z}^2}
 \end{aligned}
 \tag{30}$$

The function $f(P_m)$ in this case can be expressed as Eq. (31).

$$f(P_m) = A - 3P_m + 2P_p - \sqrt{(B - P_m)^2 + D}
 \tag{31}$$

Its first derivative can be written as

$$f'(P_m) = -3 + \frac{(B - P_m)}{\sqrt{(B - P_m)^2 + D}}
 \tag{32}$$

So far, function $f(P_m)$ and its first derivative in three cases have been obtained, and the collapse pressure of hydrate reservoir can be obtained by Newton–Raphson iteration algorithm shown in the following formula.

$$P_{m1} = P_{m0} - \frac{f(P_m)}{f'(P_m)}
 \tag{33}$$

where P_{m0} and P_{m1} are the assumed drilling fluid pressure and calculated drilling fluid pressure, respectively.

8 Appendix 2. Codes of USDFLD subroutine

C The user subroutine can determine the continuous change of physical parameters of hydrate-bearing sediments with hydrate saturation between integration points.

C This source code provides all content including code and annotation in a relatively simple way. According to this source code, simulation of related engineering geological hazards during hydrate development can be determined by other researchers.

C USDFLD subroutine will be called at each node within the investigation model to automatically determine the physical parameters.

SUBROUTINE USDFLD(FIELD, STATEV, PNEWDT, DIRECT, T, CELENT,

1. TIME, DTIME, CMNAME, ORNAME, NFIELD, NSTATV, NOEL, NPT, LAYER,

2. KSPT, KSTEP, KINC, NDI, NSHR, COORD, JMAC, JMATYP, MATLAYO, LACCFLA)

C INCLUDE 'ABA_PARAM.INC'

C CHARACTER*80 CMNAME, ORNAME

CHARACTER*3 FLGRAY(15)

DIMENSION FIELD(NFIELD), STATEV(NSTATV), DIRECT(3,3), T(3,3), TIME(2)

DIMENSION ARRAY(15), JARRAY(15), JMAC(*), JMATYP(*), COORD(*)

C T1, Peq and POR1 herein are three real variables used to store the temperature, pressure and phase equilibrium pressure of each node.

REAL T1, Peq, POR1.

C According to the temperature of each node and Eq. (5), the phase equilibrium pressure of each node can be determined.

Peq = 10**(0.034*T1 + 0.0005*T1*T1 + 6.4804).

C According to the hydrate dissociation and saturation distribution, the simulation platform will automatically determine the spatial distribution of the sediment physical parameters according to Eqs. (1) to (4).

IF (POR1.GT.Peq) THEN.

```

FIELD(1) = 2.
ELSE
FIELD(1) = 1.
END IF
RETURN
END

```

C After that, ABAQUS will automatically perform subsequent borehole stability simulations based on the updated physical parameter distribution.

Acknowledgements Implementation of the investigation should thank the theoretical support of Cheng Yuanfang's research group at China University of Petroleum (East China). At the same time, the successful publication of this paper also needs to thank to Ubedullah Ansari of Mehran University of Engineering and Technology for his help in language polishing.

Funding The authors would like to thank the research grant of Post-doctoral Program of Henan Polytechnic University (No. 712108/210).

References

1. Yao, Y.; Wei, M.; Kang, W.: A review of wettability alteration using surfactants in carbonate reservoirs. *Adv. Colloid Interfac.* **294**, 102477 (2021)
2. Yang, E.; Fang, Y.; Liu, Y.; Li, Z.; Wu, J.: Research and application of microfoam selective water plugging agent in shallow low-temperature reservoirs. *J. Petrol. Sci. Eng.* **193**, 107354 (2020)
3. Wang, Z.; Liu, X.; Luo, H.; Peng, B.; Sun, X.; Liu, Y.; Rui, Z.: Foaming properties and foam structure of produced liquid in Alkali/Surfactant/Polymer flooding production. *J. Energ. Resour. ASME.* **143**(10), 103005 (2021)
4. Shi, J.; Fan, J.; Wu, S.; Li, L.: Prediction and risk assessment of natural gas hydrate formation in deepwater wellbores. *Oil Gas Storage Transp.* **39**(9), 988–996 (2020) (in Chinese)
5. Zhang, H.; Yang, T.; Yin, H.; Lu, J.; Zhang, K.; Fu, C.: Role of Alkali type in chemical loss and ASP-flooding enhanced oil recovery in sandstone formations. *SPE Reserv. Eval. Eng.* **23**(2), 431–445 (2020)
6. Li, Q.; Liu, L.; Yu, B.; Guo, L.; Shi, S.; Miao, L.: Borehole enlargement rate as a measure of borehole instability in hydrate reservoir and its relationship with drilling mud density. *J. Pet. Explor. Prod. Te.* **11**(3), 1185–1198 (2021)
7. Milkov, A.; Sassen, R.: Estimate of gas hydrate resource, north-western Gulf of Mexico. *Mar. Geol.* **179**, 71–83 (2001)
8. Klar, A.; Soga, K.; Ng, M.: Coupled deformation-flow analysis for methane hydrate extraction. *Géotechnique.* **60**(10), 765–776 (2010)
9. Wu, N.; Zhang, H.; Yang, S.; Zhang, G.; Liang, J.; Lu, J.; Su, X.; Schultheiss, P.; Holland, M.; Zhu, Y.: Gas hydrate system of Shenhu Area, Northern South China Sea: Geochemical results. *J. Geol. Res.* **370298**, 1–10 (2011)
10. Shankar, U.; Sain, K.; Riedel, M.: Assessment of gas hydrate stability zone and geothermal modeling of bsr in the andaman sea. *J. Asian Earth Sci.* **79**(79), 358–365 (2014)
11. Zhao, X.; Qiu, Z.; Zhou, G.; Huang, W.: Synergism of thermodynamic hydrate inhibitors on the performance of poly (vinyl pyrrolidone) in deepwater drilling fluid. *J. Nat. Gas Sci. Eng.* **23**, 47–54 (2015)
12. Zhao, X.; Qiu, Z.; Sun, B.; Liu, S.; Xing, X.; Wang, M.: Formation damage mechanisms associated with drilling and completion fluids for deepwater reservoirs. *J. Petrol. Sci. Eng.* **173**, 112–121 (2019)
13. Liu, W.; Liu, R.; Zhang, M.; Liu, Z.; Lang, C.; Li, Y.: Rheological properties of hydrate slurry formed from mudflows in South China Sea. *Energy Fuels.* **35**(13), 10575–10583 (2021)
14. Lu, S.: A global survey of gas hydrate development and reserves: Specifically in the marine field. *Renew. Sust. Energ. Rev.* **41**(4), 884–900 (2015)
15. Gai, X.; Sánchez, M.: A geomechanical model for gas hydrate-bearing sediments. *J. Environ. Geotech.* **4**(2), 143–156 (2017)
16. Yan, C.; Cheng, Y.; Li, M.; Han, Z.; Zhang, H.; Li, Q.; Teng, F.; Ding, J.: Mechanical experiments and constitutive model of natural gas hydrate reservoirs. *Int. J. Hydrogen Energ.* **42**(31), 19810–19818 (2017)
17. Li, Q.; Cheng, Y.; Li, Q.; Zhang, C.; Ansari, U.; Song, B.: Establishment and evaluation of strength criterion for clayey silt hydrate bearing sediment. *Energ. Sour. Part A.* **40**(6), 742–750 (2018)
18. Song, Y.; Zhang, L.; Lv, Q.; Yang, M.; Zheng, L.; Zhao, J.: Assessment of gas production from natural gas hydrate using depressurization, thermal stimulation and combined methods. *RSC Adv.* **53**(6), 47357–47367 (2016)
19. Yun, T.: Mechanical and thermal study of hydrate bearing sediments. Ph.D. Thesis, Georgia Institute of Technology, Atlanta, USA. (2005)
20. Liu, Z.; Dai, S.; Ning, F.; Peng, L.; Wei, H.; Wei, C.: Strength estimation for hydrate-bearing sediments from direct shear tests of hydrate-bearing sand and silt. *Geophys. Res. Lett.* **45**(2), 715–723 (2018)
21. Nixon, M.; Grozic, J.: Submarine slope failure due to gas hydrate dissociation: a preliminary quantification. *Can Geotech. J.* **44**(3), 314–325 (2007)
22. Yan, C.; Ren, X.; Cheng, Y.; Song, B.; Li, Y.; Tian, W.: Geomechanical Issues in the Exploitation of Natural Gas Hydrate. *Gondwana Res.* **81**, 403–422 (2020)
23. Khabibullin, T.: Drilling through gas hydrates formations: Managing wellbore stability risks. Master thesis. Texas A&M University, Texas, USA (2010)
24. Matsuda, H.; Yamakawa, T.; Sugai, Y.; Sasaki, K.: Gas Production from offshore methane hydrate layer and seabed subsidence by depressurization method. *Eng.-PRC* **8**(6), 353–364 (2016)
25. Li, Q.; Cheng, Y.; Li, Q.; Wang, F.; Zhang, C.; Yan, C.: Investigation method of borehole collapse with the multi-field coupled model during drilling in clayey silt hydrate reservoirs. *Frattura ed Integrità Strutturale.* **12**(45), 86–99 (2018)
26. Birchwood, R.; Noeth, S.; Hooyman, P.; Winters, W.; Jones, E.: Wellbore stability model for marine sediments containing gas hydrates. In: Proceedings of American Association of Drilling Engineers National Technical Conference and Exhibition, Houston, Texas, USA, pp. 1–7 (2005)
27. Freij-Ayoub, R.; Tan, C.; Clennell, B.; Tohidi, B.; Yang, J.: A wellbore stability model for hydrate bearing sediments. *J. Petrol. Sci. Eng.* **57**(1), 209–220 (2007)
28. Salehabadi, M.: Hydrates in sediments: their role in wellbore/casing integrity and CO₂ sequestration. Ph.D. Thesis, Heriot-Watt University, Edinburgh, UK. (2009)
29. Wu, S.; Wang, J.: On the China's successful gas production test from marine gas hydrate reservoirs. *Chinese Sci. Bull.* **63**(1), 2–8 (2018) (in Chinese)
30. Chen, D.; Yao, Y.; Fu, G.; Meng, H.; Xie, S.: A new model for predicting liquid loading in deviated gas wells. *J. Nat. Gas Sci. Eng.* **34**, 178–184 (2016)
31. Yang, S.; Liang, J.; Lu, J.; Qu, C.; Liu, B.: New understandings on characteristics and controlling factors of gas hydrate reservoirs in Shenhu area on northern slope of South China Sea. *Earth Sci. Front.* **24**, 1–4 (2017) (in Chinese)
32. Zhang, G.; Chen, F.; Sha, Z.; Liang, J.; Su, X.; Lu, H.: The geological evolution process of natural gas hydrate reservoirs in the



- northeastern South China Sea. *Earth Sci. Front.* **24**, 15–23 (2017) **(In Chinese)**
33. Wu, N.; Yang, S.; Zhang, H.; Liang, J.; Wang, H.; Lu, A.: Gas Hydrate system of Shenhu Area, Northern South China Sea: Wire-line logging, geochemical results and preliminary resources estimates. In: *Proceedings of Offshore Technology Conference*, Houston, Texas, USA, (2010)
 34. Su, M.; Yang, R.; Wang, H.; Sha, Z.; Liang, J.; Wu, N.; Qiao, S.; Cong, X.: Gas hydrates distribution in the Shenhu area, northern South China Sea: comparisons between the eight drilling sites with gashydrate petroleum system. *Geol. Acta.* **14**(2), 79–100 (2016)
 35. Lu, Y.; Luan, X.; Lyu, F.; Wang, B.; Yang, Z.; Yang, T.; Yang, Z.: Seismic evidence and formation mechanism of gas hydrates in the Zhongjiannan Basin, Western margin of the South China Sea. *Mar. Petrol. Geol.* **84**, 274–288 (2017)
 36. Zhang, H.; Lu, H.; Liang, J.; Wu, N.: The methane hydrate accumulation controlled compellingly by sediment grain at Shenhu, Northern South China Sea. *Chin. Sci. Bull.* **61**(3), 388–397 (2016)
 37. Zhou, S.; Zhao, J.; Li, Q.; Chen, W.; Zhou, J.; Wei, N.; Guo, P.; Sun, W.: Optimal design of the engineering parameters for the first global trial production of marine natural gas hydrates through solid fluidization. *Nat. Gas Ind. B.* **5**(2), 118–131 (2018) **(In Chinese)**
 38. Yan, W.; Huang, L.; Wang, D.: Deepening oceanic scientific research in the South China Sea is the major strategic demand of the development of China. *Bull. Chinese Acad. Sci.* **3**(2), 121–126 (2008) **(In Chinese)**
 39. Liu, M.; Jin, Y.; Lu, Y.; Chen, M.; Hou, B.; Chen, W.; Wen, X.; Yu, X.: A wellbore stability model for a deviated well in a transversely isotropic formation considering poroelastic effects. *Rock Mech. Rock Eng.* **49**(9), 3671–3686 (2016)
 40. Sun, S.; Ye, Y.; Liu, C.; Xiang, F.; Ma, Y.: P-T stability conditions of methane hydrate in sediment from South China Sea. *J. Nat. Gas Chem.* **20**(5), 531–536 (2011)
 41. Li, Q.; Cheng, Y.; Li, Q.; Ansari, U.; Liu, Y.; Yan, C.; Lei, C.: Development and verification of the comprehensive model for physical properties of hydrate sediment. *Arab. J. Geosci.* **11**(12), 325 (2018)
 42. Su, Z.; Moridis, G.; Zhang, K.; Yang, R.; Wu, N.: Gas Hydrate: Numerical investigation of gas production strategy for the hydrate deposits in the Shenhu Area. In: *Proceedings of Offshore Technology Conference*, Houston, Texas, USA, (2010)
 43. Wang, X.; Hutchinson, D.; Wu, S.; Yang, S.; Guo, Y.: Elevated gas hydrate saturation within silt and silty clay sediments in the Shenhu area, South China Sea. *J. Geophys. Res.-Sol. Ea.* **116**(B5), B05102 (2011)
 44. Xiao, K.; Zou, C.; Xiang, B.; Liu, J.: Acoustic Velocity Log Numerical Simulation and Saturation Estimation of Gas Hydrate Reservoir in Shenhu Area South China Sea. *Sci. World J.* **101459**, 1–13 (2013)
 45. Liu, J.; Zhang, J.; Sun, Y.; Zhao, T.: Gas hydrate reservoir parameter evaluation using logging data in the Shenhu area South China Sea. *Nat. Gas Geosci.* **28**(1), 164–172 (2017) **(in Chinese)**
 46. Wang, X.; Wu, S.; Yang, S.; Liang, J.; Guo, Y.; Gong, Y.: Gas hydrate occurrence, saturation and geophysical signatures associated with flow in silt-dominated reservoirs. In: *Proceedings of the 7th International Conference on Gas Hydrates*, Edinburgh, Scotland, United Kingdom, (2011)
 47. Wan, Z.; Wang, X.; Xu, X.; Guo, H.: Control of marine geothermal field on the occurrence of gas hydrates in northern South China Sea. In: *Proceedings of 2016 SEG International Exposition and Annual Meeting*, Dallas, Texas, USA, (2016)
 48. Zhang, H.; Cheng, Y.; Shi, J.; Li, L.; Li, M.; Han, X.; Yan, C.: Experimental study of water-based drilling fluid disturbance on natural gas hydrate-bearing sediments. *J. Nat. Gas Sci. Eng.* **47**, 1–10 (2017)

